Electronic Supplementary Material (ESI) for Lab on a Chip.

Supplementary Materials: Finger-Powered Fluidic Actuation and Mixing via MultiJet 3D Printing

Eric Sweet*, Rudra Mehta, Yifan Xu, Ryan Jew, Rachel Lin and Liwei Lin

1. Detailed Design Dimensions

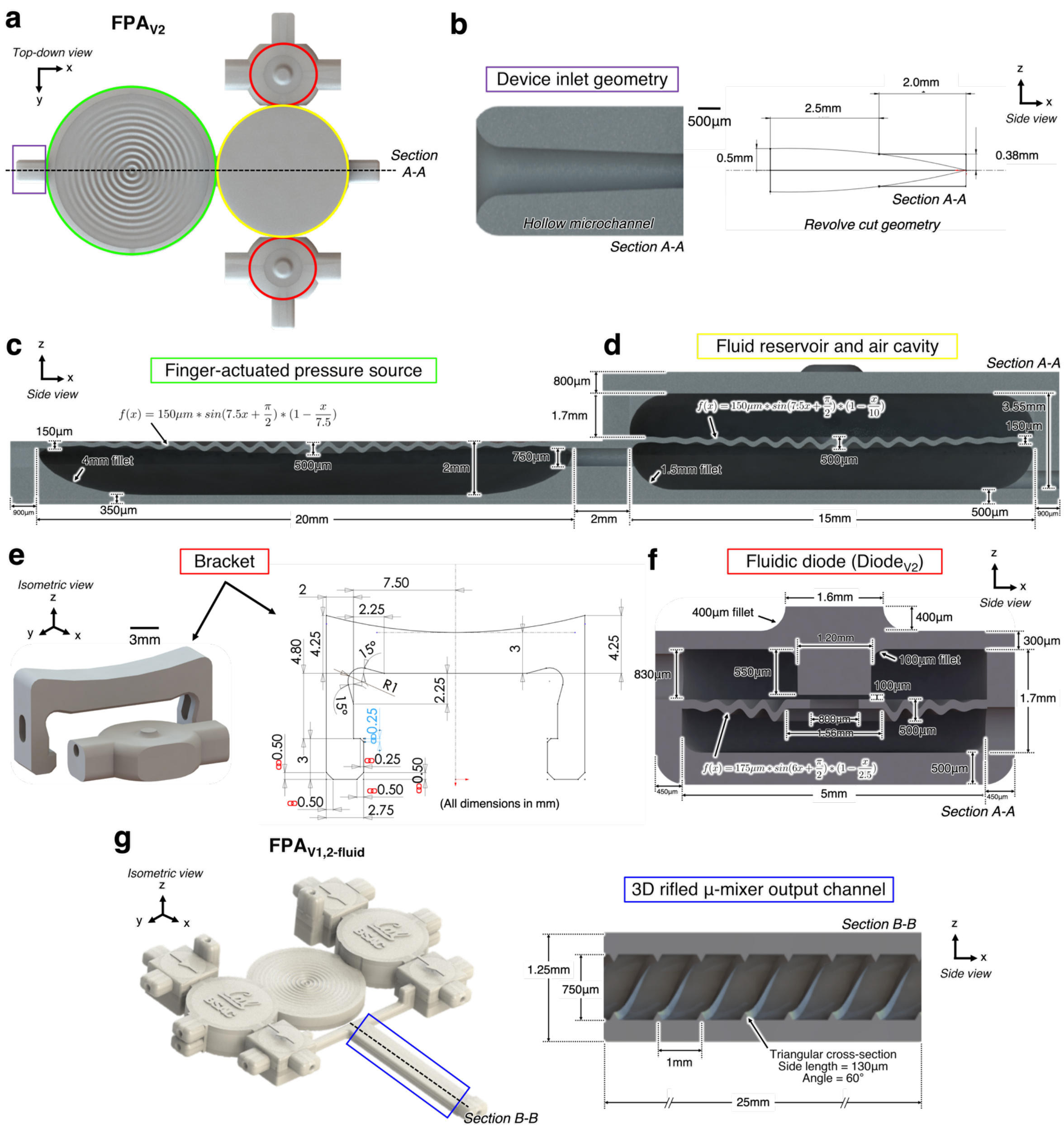

Figure S1. Detailed dimensions of 3D fluidic operator designs, cross-sections of 3D solid model renderings shown. **(a)** FPA$_{V2}$ indicating device inlet geometry (*purple*), finger-actuated pressure source (*green*), fluid reservoir and air cavity *yellow*), and fluidic diodes (Diode$_{V2}$, *red*). **(b)** Device inlet geometry, hollow microchannel rendering (*left*) and revolve cut geometry (*right*). **(c)** Finger-actuated pressure source (*green*) and **(d)** air cavity *yellow*). **(e)** Modular bracket enabling diode mechanism. **(f)** Diode$_{V2}$ with bracket *off*. **(g)** FPA$_{V1,2fluid}$ (*left*) indicating 3D rifled μ-mixer output channel (*right*).

2. Experimental Setup

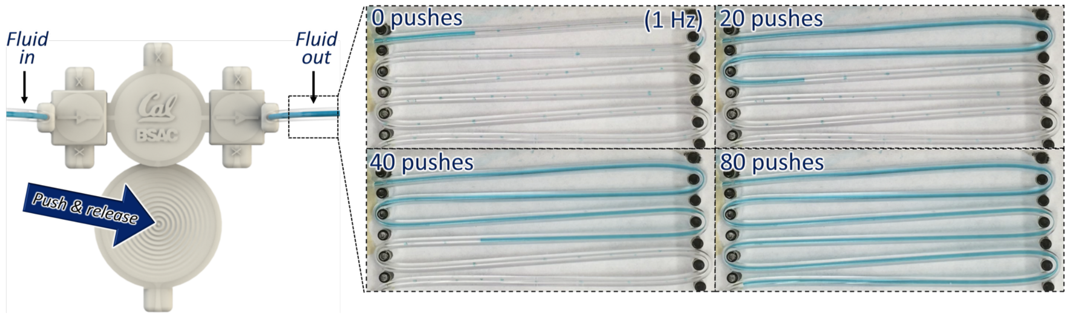

Figure S2. Experimental visualization of fluid actuation results from the single-fluid FPA prototype. (*Left*) Rendering of the fabricated prototype indicating the locations of the fluidic input and output from the device and the push-and-release operation on the finger-actuated pressure source. (*Right*) Actual blue dyed fluid output from the device filling transparent tubing resulting from device operation at one push-per-second (*i.e.* 1 Hz pushing frequency). Device output volume corresponding to 0, 20, 40 and 80 pushes on the finger-actuated membrane.

Figure S3. Example experimental setup visualizing fluid output from an FPA$_{V1}$ prototype with actuation at 1 Hz. A ruler placed above the tubing served as a length reference. White paper underneath the setup provided maximum contrast between the colored output fluid and the background.

2.1. Further Discussion on the Experimental Setup

To evaluate the fluid actuation performance of each fabricated FPA prototype, a bench top setup was constructed and used to visualize the forward-driven fluid output from each device upon actuation of the finger-actuated pressure source membrane. An example of the experimental setup used to test the fabricated FPA$_{V1}$ prototype is shown in Figure S2,S3.

Before each experiment involving the single-fluid FPA prototypes, blue dyed solution, which was formulated by filling a 10mL glass petri dish with DI water and adding and incorporating 10 drops of blue food-grade color dye, was used to prime (pre-load) each prototype device. Briefly, a 10mL syringe attached to a 20-gauge Luer stub was used to fill the entirety of the fluidic network with the dye solution. The syringe was filled with blue dyed fluid, then attached to one device inlet at a time. A slight pressure to the manually depressed syringe plunger was applied until fluid entered the microchannel network, as visible through the semi-transparent material, being careful not to apply excess force as to generate fluidic pressure as to visibly displace the internal 3D corrugated membranes, but sufficient pressure as to fill the entirety of each microchannel and eliminate air bubbles. Fluid was first input into the overall device inlet to the top channels of the left-most fluidic diode, until the fluid exited the adjacent inlet to said channel, eliminating any air bubbles, as well as flowed through the aperture in the internal 3D corrugated membrane and filled the lower channel of the diode. Fluid was then used to fill the lower channel of the diode, forcing any remaining air bubbles in the lower channel out of the diode through the opposing inlet, until the fluid flowed out of the lower channel and into the fluidic reservoir. Fluid was then input to the fluid reservoir, filling the entirety of the chamber and forcing fluid into the upper channel of the right-most fluidic diode. Fluid was then input into the inlet to the upper channel of the diode until the fluid filled the channel, then flowed through the aperture in the 3D corrugated membrane to fill the lower channel of the diode. Fluid was then input into the inlet to the lower channel of the diode until all remaining air bubbles were removed and forced out of the overall device outlet of the lower channel. All device inlets, other than the overall device inlet (to the upper channel of the left-most diode) and overall device outlet (to the lower channel of the right-most diode), were blocked using stainless steel catheter plugs (#SP20/12, *Instech*).

In the experiments involving the two-fluid FPA$_{V1,2fluid}$ prototype, blue dyed solution and yellow dyed solution were used to fill each independent fluid network until laminar flow exited the terminus of the linear output channel. Segments of Tygon microbore tubing (model #06420-03, *Cole-Palmer*) were then connected to each inlet *via* stainless steel interconnecting couples (model SC20/15, *Instech*). The other end of the short segment of tubing ($\sim$1 cm) connected to the inlet of the prototype device (pre-filled with blue solution) was connected to a 3D printed 5mL reservoir filled with blue dyed fluid and serving as the fluidic source. The longer segment of tubing (up to $\sim$50 cm) connected to the outlet of the prototype device was used to visualize the output fluid from the device. To seal the air pressure source, steel plugs were used to block the two microchannel inlets to the pressure source channel. The experimental setup for each test consists of a white printer paper background to provide maximum contrast between the blue fluid filling the tubing and the background surface and the output segment of tubing linearly-positioned with a ruler placed above the tubing serving as a length reference.

3. Fabricated Prototype Images

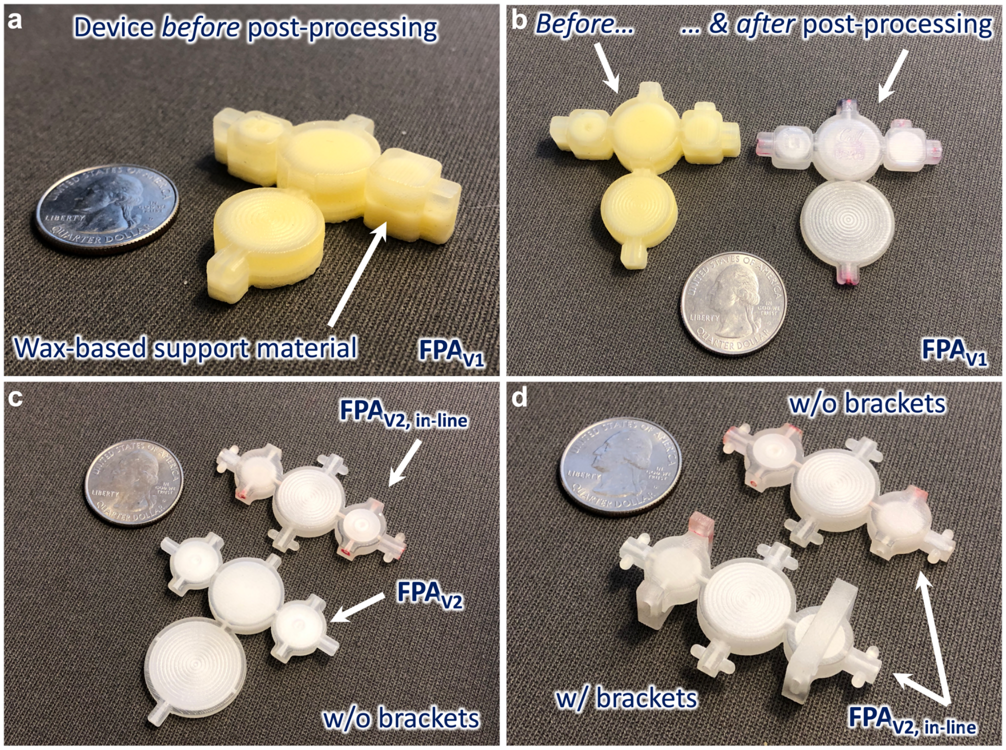

Figure S4. 3D printed fabrication results. **(a-b)** FPA$_{V1}$, **(c)** FPA$_{V2}$, **(d)** FPA$_{V2,in-line}$

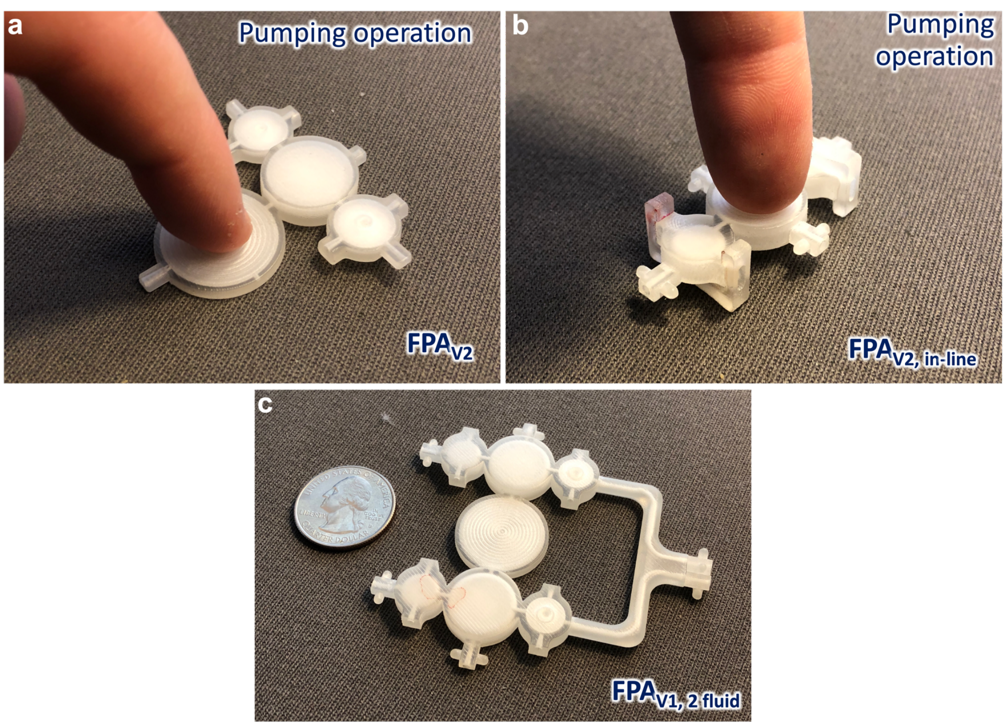

Figure S5. 3D printed fabrication results, FPA prototypes showing finger-powered actuation. **(a)** FPA$_{V2}$, **(b)** FPA$_{V2,in-line}$, **(c)** FPA$_{V1,2fluid}$.

4. Expanded Data Acquisition and Video Analysis Protocols

4.1. Video Analysis

A video analysis approach was chosen for data acquisition. It was experimentally-determined upon initial interfacing of the fluid output of the fabricated FPA prototypes that the rate of change of the instantaneous flow rates from the prototype devices at 1 Hz. Higher actuation frequencies exceeded the measurement capabilities of the FLOWELL microfluidic flow rate sensor platform (*Fluigent*) used in the laboratory for data acquisition. Since the sampling rate of an iPhone camera (30 frames-per-second) is higher than that of the FLOWELL platform (10 samples-per-second), a video recording method was employed to acquire raw data of the fluidic output performance of each prototype with different actuation frequencies. The operation of each prototype was recorded at 30 frames per second using an iPhone 10 camera running the iOS 11 operating system, and the video recording was subsequently analyzed using a custom Python video analysis script. The iPhone camera was supported using foam blocks to either side of the experimental setup, outside of the frame of the camera and positioned such that no shadow effects were generated. The lighting source was provided by an incandescent light bulb on a standing lamp positioned to the side of the iPhone as to deliver uniform light directed down upon the output tubing with no shadows or brilliant reflection on the tubing itself. Default frame rate, zoom and exposure settings for the iPhone 10 camera were used.

When the video recording was manually-started, a digital iPhone metronome app (Pro Metronome, *Xanin Tech, GmbH.*) was used to produce a sound at the desired frequency, and the prototype was then manually-actuated to match the desired actuation frequency produced by the metronome app, pushing with the pad of the index finger until the membrane was fully-depressed and being careful not to apply excess pressure to the sides of the membrane where the material is the weakest, which could result in fracture. The experiments all run for up to one minute, or until the output tubing is completely filled (at higher Hz). When complete, the video recording is ended and the video file transferred to a computer and used in the following video analysis procedure. Analysis of the video recordings served to quantify fluid output parameters such as instantaneous fluid flow rate (one measurement every $\sim$33 milliseconds); average effective fluid flow rate over the course of the recording; the forward, reverse and net volume pumped per actuation cycle and with respect to time and with respect to actuation frequency.

To analyze the fluid output performance of the fabricated FPA$_{V1}$, FPA$_{V2}$ and FPA$_{V2,in-line}$ prototypes, a combination of image processing using Fiji image analysis software and data analysis using a custom Python script were employed to extract raw data from each frame of a video recording of a given prototype operation experiment and to produce and plot the aforementioned quantifiable fluid flow parameters. Briefly, a raw .MOV video is imported into Fiji image analysis software, where it is then manually trimmed to appropriate beginning and ending times, the measurement scale is defined based on the size of a ruler in the frames of the video, an RGB stack is performed and the red channel selected and built-in software tools used to create a vectorized skeleton of the fluid path throughout the duration of the video. This skeleton (.txt file) along with video frames (.png files) at the beginning and ending of the video are then saved. The Python script is then used to import the skeleton, video frames and the video file itself. The program then analyzes the video to calculate the distance that the fluid has traveled along the path length of the tube at each frame of the video, then a a series of image processing codes calculate the instantaneous fluid flow rate and volume pumped at each frame (one-thirtieth of a second), taking into account the inner diameter of the tubing, and storing this data in a matrix. This data is then processed to plot all quantified fluid flow parameters.

To run this protocol, you'll need the following programs/packages:

- Python
  - Numpy
  - Matplotlib
- ImageJ
- OpenCV
- FFMPEG

Step 1. Obtain video of test as a `.mov` file. Find the number of pumps and save this value

Step 2. Trim the video to the desired start/stop times

Step 3. Convert the video to a raw `.avi` file

a. Run the following command from terminal:

```
ffmpeg -i [input_name].mov -an -vcodec rawvideo -filter:v
fps=30 -y [output_name].avi
```

b. Place the `.avi` file in a folder named `[output_name]`. This name will be referred to as `video_name` from here on.

Step 4. Open the `.avi` file with ImageJ as a stack

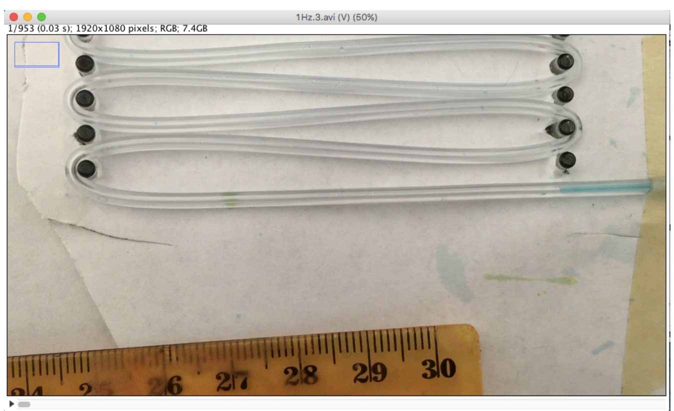

Step 5. Draw a line between 2 of the cm marks on the ruler, and press `m` to measure it. Grab the pixel distance reported, and convert it to a µm/pixel ratio. Save this value for later.

Step 6. [ImageJ] Crop video to region of interest (Note: takes a while for long videos)

Step 7. [ImageJ] Split channels, keep the red channel window, close the others. Save this as an AVI, no compression, with the name `[video_name]_r.avi`.

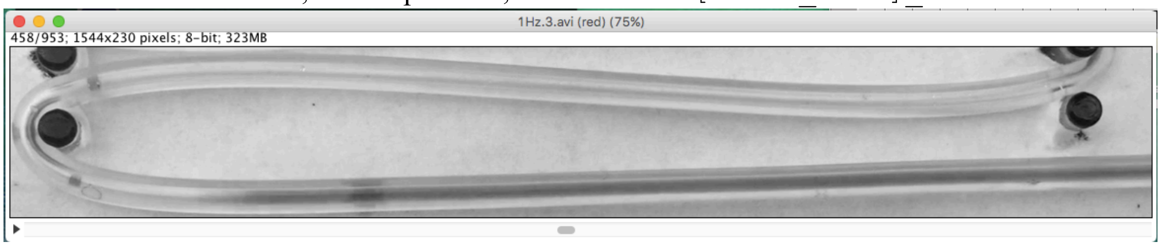

Step 8. [ImageJ] Save the first time slice as a PNG, and save the time slice where the fluid goes the farthest as another PNG. Then open both with ImageJ.

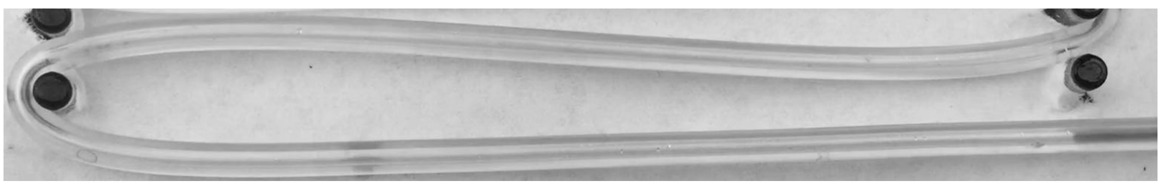

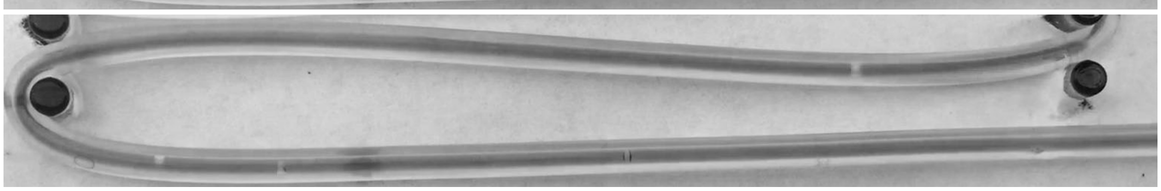

Step 9. [ImageJ] Go [Process]→[Image Calculator] and select the 'Difference' option.

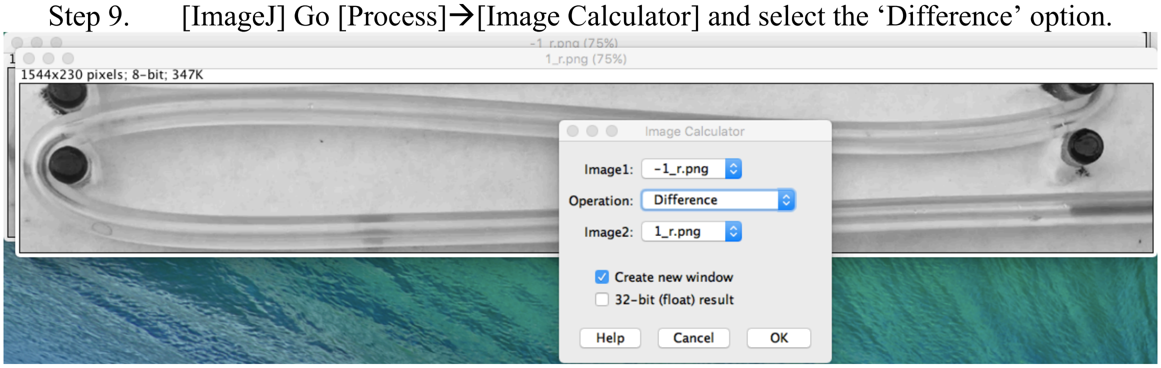

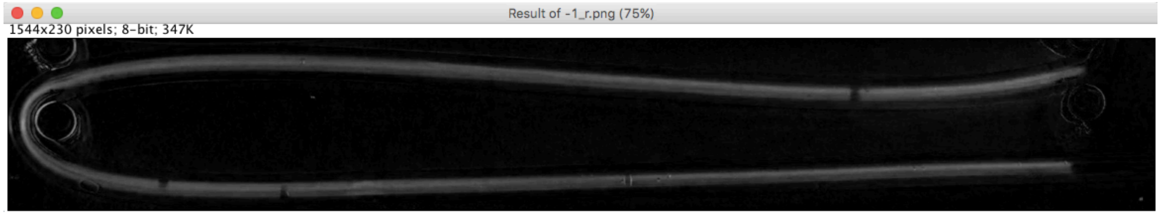

Step 10. [ImageJ] On the resulting image, go [Process]→[Binary]→[Make Binary]. You should see a white line, though the image might have some other white areas and the line might not be fully connected.

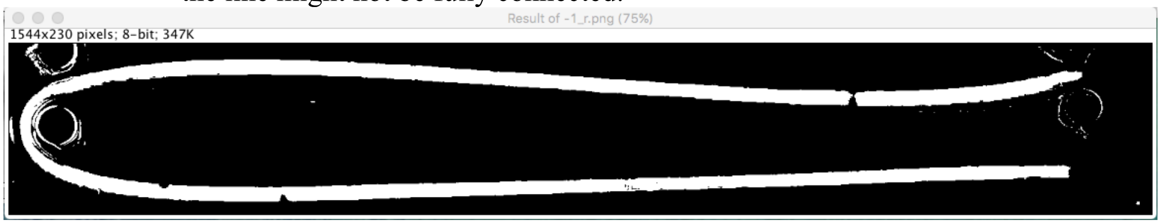

Step 11. [ImageJ] Go to color picker, and click on a white region of the image. Then, select the pencil tool, and draw in lines to connect the line.

Then if you go [Process]→[Binary]→[Fill Holes], it should result in one pure white line.

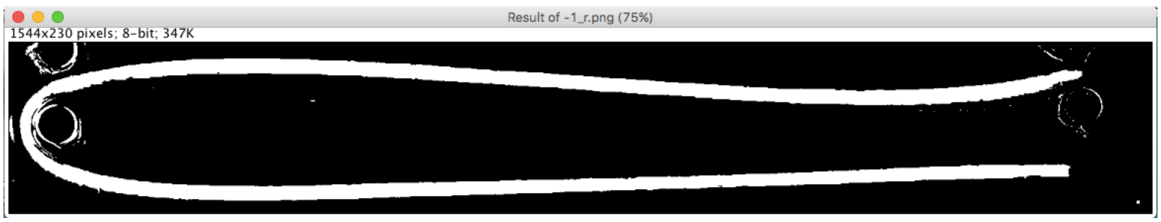

Step 12. [ImageJ] Go [Process]→[Binary]→[Open], then [Process]→[Binary]→[Dilate], and finally [Process]→[Binary]→[Skeletonize] to get a skeleton (single pixel-wide line) of the path the fluid takes in the video. However, the skeleton isn't perfect yet; we have to clean it up.

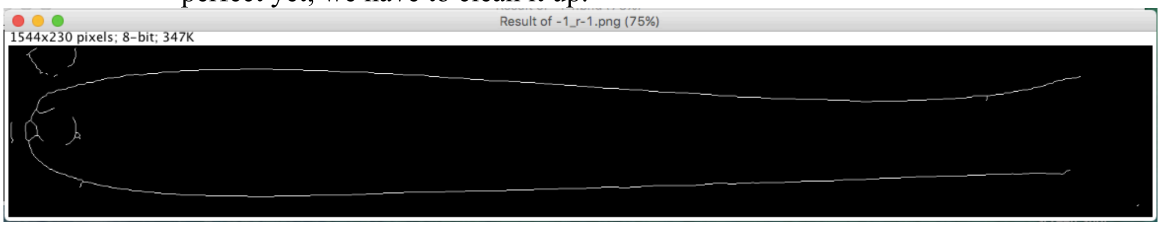

Step 13. [ImageJ] Using the drawing tools, clean up the skeleton. You should only be left with one white line (one pixel thick in all places). Each white pixel should be touching exactly 2 other white pixels when you look at all 8 contact points (edges + corners), excluding the first and last white pixel in the path. Also, extend both the beginning and ending of the path by at least 10 pixels.

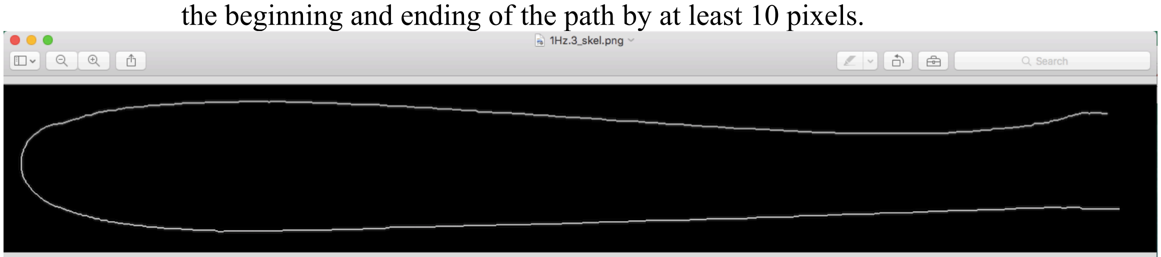

Save this skeleton as both a PNG and Text Image. The names should be `[video_name]_skel.png` and `[video_name]_skel.txt`

Step 14. [ImageJ, Python] Figure out the x,y coordinates of the first point in the path. Open the python file `FPP_skeleton.py` and locate the `valsPerVid` dictionary at the top. Add an entry to the dictionary, with the format

`"[video_name]":([x-coord],[y-coord])`

and filling in the regions inside the [ ]. Additionally, change the variable `name` to the `[video_name]` you entered in the dictionary.

```
# name : initial point (x,y)
valsPerVid = { "test1":(345,519), "1Hz.3":(1474,164)}

# Change this line for each video
name = "1Hz.3"
```

Step 15. [Python] Run `FPP_skeleton.py`. Make sure the equality printed out makes sense, or else you have an error in your skeleton. If you do, the smaller number is the pixel where something went wrong. Usually, the issue will be that you have an extra pixel along the path in that location.

```
[calvisitor-10-105-164-142:fpp rudramehta$ python FPP_skeleton.py
2929 == 2929?
```

Step 16. [Python] Next, open `FPP_analyze.py`. Again, locate the `valsPerVid` dictionary at the top, and add another entry. This time, the format is

```
"[video_name]":[image_threshold]
```

Image threshold is the pixel brightness value that the program will use to determine if a given pixel contains fluid or not. You can determine this value by opening the [video_name]_r.avi file you saved in ImageJ, and inspecting pixel values for pixels containing and not containing fluid, and select an appropriate threshold from there. Run `FPP_analyze.py`.

```
# name : threshold
valsPerVid = { "test1":125, "1Hz.3":50 }

# Change this line to choose a video
name = "1Hz.3"
```

Step 17. [Python] Finally, open `FPP_graph.py`. Locate the `valsPerVid` dictionary at the top, and add another entry. This time, the format is

```
"[video_name]":([num_pumps],[µm_per_pixel])
```

where `num_pumps` and `µm_per_pixel` are from steps 1 and 2, respectively.

```
# name : (number of pumps, um per pixel)
valsPerVid = { "test1":(83, 84), "1Hz.3":(29,51.26)  }

# Change this line for each video
name = "1Hz.3"
```

Step 18. Run `FPP_graph.py`. The result will be placed in the folder you created in step 3.

To change the results displayed:

If you want to see different results, you can edit the file `FPP_graph.py`. It relies on a lot on Numpy and Matplotlib to create the graphs.

How it works:

The file's input is an array called `lens`. `lens` contains the length that the flow travelled, in pixels, every frame. Using `µm_per_pixel` and `radius`, these values are converted to µL pumped per frame. Furthermore, using `fps` (frames per second` when graphing, you can get a graph of Volume pumped (µL) vs Time (s).

Other possibilities with data:

Another thing you can do with the data is use numpy's gradient function to generate a derivative. If this is done after the unit conversion to get `lens` to a volume, you can graph the gradient vs time to get a Volume Flow Rate (µL/s) vs Time (s) graph.

You can also use the `num_pumps` value to plot Volume pumped (µL) vs Push.

To produce the Mixing Index values for the fabricated FPA$_{V1,2fluid}$ two-fluid mixer prototype, device actuation at 1 Hz for a period of 10 seconds was recorded, centering the video on the output microchannel section of both smooth-walled control and μ-mixer integrated channel prototypes. The final frame of each video was then selected, manually imported into Fiji image analysis software, and the image analysis procedure was employed to quantify mixing at the terminus of the microchannel outlet section. Three experimental mixing demonstrative experiments were performed and the mean Mixing Index, along with the standard deviation between experiments, were calculated.

4.3. Protocol For Producing RMI Value, Image Analysis and Calculations

The metric used to quantify the degree of fluidic mixing at the terminus of the linear microchannel attached to the two-fluid FPA$_{V1,2fluid}$ prototype following 10 seconds of actuation at 1 Hz, the Relative Mixing Index (RMI) value, or Mixing Index, has been demonstrated extensively by previous work [1–7] to be a standard metric by which to quantify the mixing quality inside microchannels of various morphologies from both fluorescence and non-fluorescence imaging. For each experimental prototype outlet configuration: attached to a smooth-walled linear microchannel region (control experiment) and attached to a 3D rifling-walled linear microchannel region (3D μ-mixer experiment); three experimental videos are analyzed.

In Fiji software (an open-source distribution of ImageJ image processing software):

1. Open the video recording in Fiji.
2. Isolate the final frame of the video.
3. Open ROI Manager.
4. Create an RGB stack of the image and select the Green stack.
5. Draw a square before the entrance of the linear microchannel, where both blue and yellow fluids are present before they combine to form co-laminar flow. Ensure that the drawn height of the square is no taller than the width of the microchannel.
6. A Python script is created and loaded into the Macros programming extension on Fiji that enables automated data collection. In the ROI manager, run this script, which records the intensities of the pixels across the isolated area, storing them in a two-dimensional matrix in a .csv file.
7. In the ROI Manager, draw another square on the terminus of the microchannel with roughly the same dimensions as the initial square, capturing the mixing quality of the co-laminar fluids at the outlet, and run the script again.
8. In order to account for the variation in the data from the specific dimension of rectangle drawn and the positioning on the image, repeat the preceding steps twice more (draw rectangle and run script) to have three separate measurements of the inlet and outlets of the device.
9. Repeat the above steps for each video.

In Python:

1. Run a Python script that was created to calculate the RMI value for a single experiment.
2. Change the input directory of the Python script to the folder containing all of the .csv files for a given experiment.
3. Run the script, which performs the calculations as described in the following section, to calculate the RMI value by calculating RMI from each pixel value stored in the Fiji Macros-exported matrix.
4. Repeat the above procedure to analyze all data for a single device configuration, generating three RMI values.
5. Use an additional custom Python script to calculate the average RMI value for that device configuration and the standard deviation, then plot the data.

The RMI value is computed for the selected frame of each experimental video as the ratio of the standard deviation of the pixel intensities at the terminus of the linear microchannel (σ) to the standard deviation of the pixel intensities at the start of the microchannel (σ_o), as calculated by Eq. 1 [7]

$$RMI = 1 - \frac{\sigma}{\sigma_o} = 1 - \frac{\sqrt{\frac{1}{N}\sum_{i=1}^{N}(I_i - < I >)^2}}{\sqrt{\frac{1}{N_o}\sum_{i=1}^{N_o}(I_{io} - < I_o >)^2}} \tag{1}$$

where I_i is the intensity of each pixel inside the drawn rectangle at the terminus of the microchannel, $< I >$ is the average value of the local pixel intensities in said rectangle, N is the number of the pixels inside said rectangle, I_{io} is the intensity of each pixel inside the drawn rectangle at the beginning of the microchannel, $< I_o >$ is the average value of the local pixel intensities in said rectangle, and N_o is the number of the pixels inside said rectangle. The RMI value quantifies the mixing quality as a decimal value 0 to 1, where a value of 0 corresponds to completely unmixed fluids (at the inlet to the co-laminar flow microchannel) while a value of 1 corresponds to fluids in a completely mixed state. However, a percentage (100**RMI*) can also be used to describe the quality of mixing as in *how well mixed is the fluid compared to being 100% completely mixed (quantitatively defined in quantitative processing), relative to the 0% mixing of the two initially-discrete fluidic species* [8].

5. Additional Experimental Data for FPA$_{V1}$

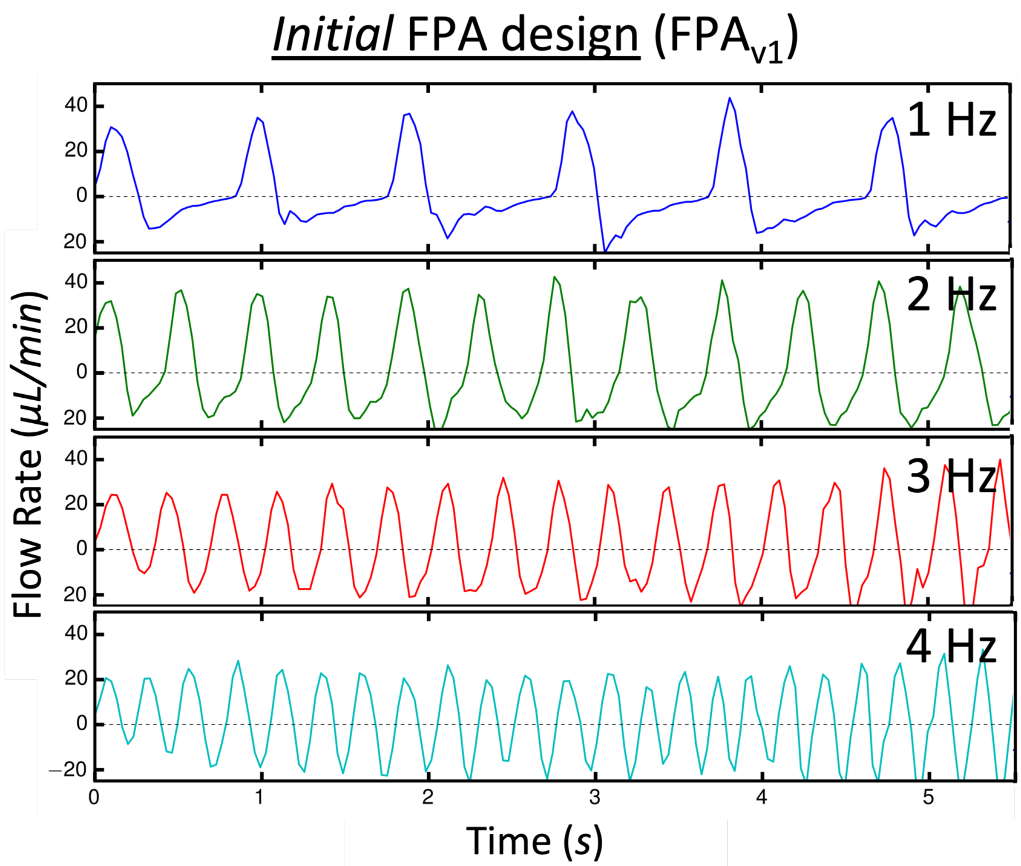

Figure S6. FPA$_{V1}$, instantaneous flow rate vs. time for 1-4 Hz.

6. Further Details on the 3D Fluidic Diode Designs

6.1. Initial Design, Diode$_{V1}$

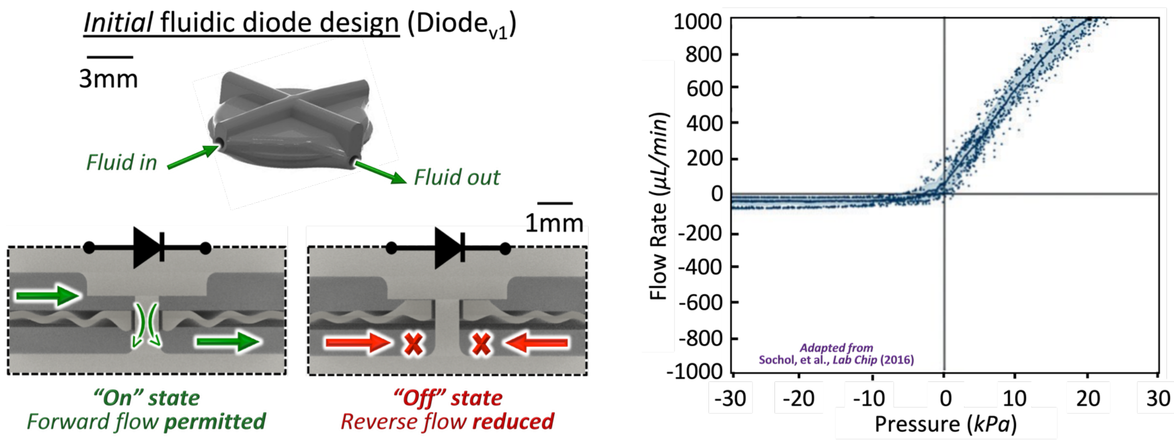

Figure S7. Design and experimental Q-P diagram of Diode$_{V1}$, previously published by our group in Sochol et al., *Lab Chip*, 2016 [9]. **(a)** Isometric view rendering of a modular Diode$_{V1}$ with four inlets for support material removal (*top*) and cross-section renderings of the interior of Diode$_{V1}$. In the *on* state (*bottom left*), a positive pressure (*i.e.* positive pressure into the upper fluid channel) drives fluid through the circular aperture in the corrugated membrane from the upper to the lower channel and deflects the membrane downwards, resulting in forward flow through the diode; in the *off* state (*bottom, right*), a negative pressure (*i.e.* positive pressure into the lower fluid channel) deflects the membrane upwards until contact is made with the upper surface, effectively closing the gap and reducing reverse flow through the diode. **(b)** Experimental Q-P diagram [9] showing output flow rates from Diode$_{V2}$ resulting from forward and reverse pressure sweeps in triplicate experiments, moving average trend line and standard deviation, demonstrating experimental diodicity of $\sim$80.6.

The *initial* fluidic diode (Diode$_{V1}$) employed by the FPA$_{V1}$ prototype was based on the 3D fluidic diode design previously developed by our group [9]. Briefly, the enclosed 3D corrugated membrane isolates upper and lower microchannels, and a protruding cylinder in the upper channel provides a smaller clearance with the membrane in the upper channel (200 μm) than in the lower channel (700 μm). The membrane consists of a central (800 μm diameter) thru-hole surrounding a concentric (600 μm diameter) pillar, forming an annular aperture. When the pressure difference between the upper and lower channels, ΔP, is positive (ΔP>0), the membrane is deformed downwards and fluid flows through the annular aperture, into the lower channel and out of the diode. When ΔP<0, the membrane is deformed upwards, making physical contact with the upper surface and obstructing fluid flow through the aperture. As a result, the diode provides lower fluidic resistance in the forward direction (*i.e.* fluid flow from the upper to the lower channel) than in the reverse direction (*i.e.* fluid flow from the lower to the upper channel) and therefore flow rectification, whereby fluidic resistance is dependent on various physical parameters including the area of the annular aperture, the flexural rigidity of the polymer and the clearance between the aperture and the opposing face when ΔP=0, in addition to the fluidic viscosity and magnitude of ΔP. Fabricated Diode$_{V1}$ prototypes [9], and as a result FPA$_{V1}$ in this work, demonstrated lower fluidic resistance and fluid flow rectification, i.e. $Vf{:}Vr > 1$, in the forward direction, albeit with considerable back-flow. The results of experimental fluid rectification characteristics of a fabricated Diode$_{V1}$ prototype are presented in Figure S7b (plot adapted from the figure in our group's previous publication [9]) as a flow rate *versus* pressure (QP) plot, which is the hydrodynamic equivalent of a current-voltage (IV) curve which is used to examine the electrical current rectification behavior of an electrical diode. The fabricated Diode$_{V1}$ prototype generates forward fluid flow rates up to $\sim$ 800 μL/min at $\sim$15 kPa, while permitting back-flow regardless of the magnitude of the applied negative pressure with flow rates up to 45 kPa in the reverse direction due to applies negative pressure up to ∼30 kPa. Furthermore, the prototype demonstrated a diodicity value of ∼80.6.

6.2. Improved Design, Diode$_{V2}$

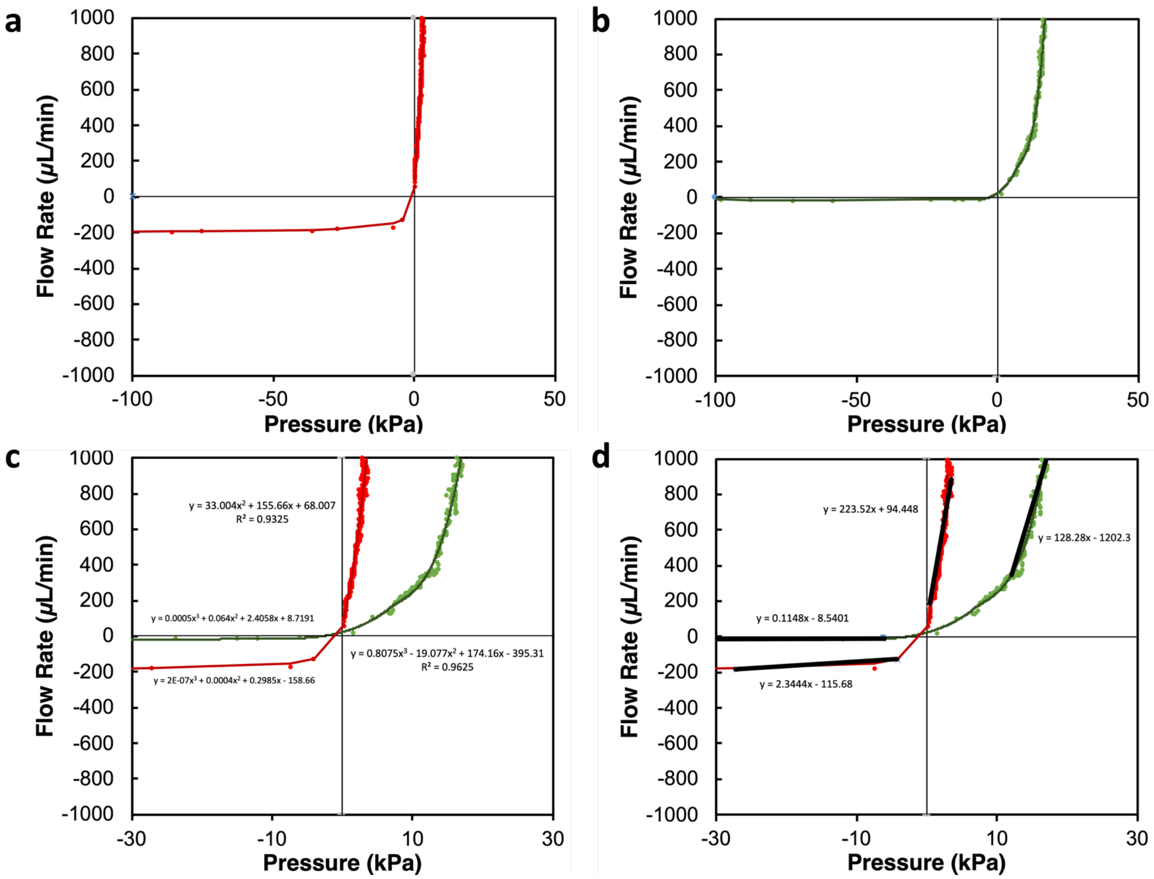

Figure S8. Additional visualization of Diode$_{V2}$ experimental characterization results, Q-P plots. **(a)** Diode$_{V2}$ with bracket off. **(b)** Diode$_{V2}$ with bracket on. **(c)** Diode$_{V2}$ both states showing equations of approximate lines of best fit. **(d)** Diode$_{V2}$ both states showing equations of approximate linear lines of best fit for calculation of diodicity

A conceptual Diode$_{V2}$ consists of two distinct elements, the 3D fluidic diode itself, as well as a modular *bracket* component. The interior of the fluidic diode, similar to the interior of Diode$_{V1}$, entails a dynamic 3D corrugated membrane with a 1 mm diameter central circular aperture which divides upper and lower fluid channels. Additionally, upper surface extends deeper into the upper channel to within an as-fabricated clearance of 100 μm of the upper surface of the dynamic membrane, whereas the lower surface of the interior of the diode has a clearance of 750 μm from the bottom of the membrane. Notably, this design lacks a central column (as is featured in the interior of Diode$_{V1}$) in order to permit lower fluidic resistance through the central aperture. Therefore when the bracket is in the *off* position, not installed on the diode, the as-fabricated clearance permits forward and reverse flow dynamics similar to those inherent to the the Diode$_{V1}$ design. Unique to Diode$_{V2}$, however, is the raised knob on the upper exterior surface of the diode. When the bracket is in the *on* position, installed on the diode (holes on each side of the bracket permit interfacing with the inlet and outlets of the diode using standard steel couples), the lower surface of the bracket contacts and depresses the knob on the upper surface of the diode (since the two surfaces overlap by 150 μm and the 5 mm thick bracket is much more rigid than the ∼500μm thick upper surface of the diode). Therefore the upper surface of the diode, and subsequently the protruding structure in the upper channel, is displaced downwards until the clearance between the membrane and the protruding structure is effectively eliminated. As a result, in the default fluidic state at P = 0 (*i.e.* equivalent fluid pressures in the upper and lower channels), back-flow through the aperture is prevented by the absence of clearance on the upper surface of the membrane. Therefore with the bracket installed, under positive pressure ($P > 0$), an initial threshold pressure value must be reached in order to apply sufficient force on the membrane in order to cause downwards displacement and permit forward fluid flow through the aperture. Under negative pressure however ($P < 0$) or at P = 0, the energy stored in the displaced membrane due to elastic strain restores the membrane back to its initial position, passively-eliminating the clearance between the membrane and the protruding surface which exists only under sufficient positive applied pressure, and preventing further back-flow in the system and rectifying reverse fluid flow more effectively than the closure mechanism of the Diode$_{V1}$ design. Finally, comparing the QP data for both Diode$_{V1}$ and Diode$_{V2}$ designs reveals that the passive fluid rectification mechanism employed by Diode$_{V2}$ with the bracket installed is more effective than the dynamic fluid rectification mechanism employed by Diode$_{V1}$. The maximum back-flow in Diode$_{V1}$ reaches $\sim$45 μL/min at $\sim$30 kPa negative pressure, whereas the back-flow in Diode$_{V2}$ reaches only $\sim$12 μL/min at $\sim$30 kPa negative pressure, demonstrating an $\sim$73.4% improvement in back-flow reduction as compared to Diode$_{V1}$.

6.3. A Note on Why Diode$_{V2}$ Requires a Modularly Fabricated Bracket

Employing modular bracket elements to the Diode$_{V2}$ operators yields improved fluid rectification performance over the as-fabricated structure. A potential point of inquiry might naturally follow that the impact of the entire FPA platform to be monolithically fabricated would be apparently diminished by the fact that the Diode$_{V2}$ designs necessitate the use of modular components in order to properly function.

To clarify, the manner in which the DiodeV2 3D fluidic diode operator is fabricated, in fact represents the only practical manner in which a "normally closed" microscale valving element can be manufactured, as monolithically as possible. The general approach to fabricating conventional microfluidic "normally closed" valve structures, such as those employed in typical lab-on-a-chip microfluidic systems, involves manufacturing of discrete material layers (e.g., multi-layer PDMS or PMMA bodies with intra-layer membranes) followed by manual assembly and bonding to form a complete structures with dynamic valves which are in the "closed" position by default and only "open" to permit fluid flow when subjected to a positive forward driving fluidic pressure [10,11].

Indeed, the 3D printed DiodeV2 operator is currently monolithically fabricated without the bracket, and as a result, the internal valving mechanism consists of a 100 μm clearance between the internal 3D corrugated membrane and the upper surface inside the 3D fluidic DiodeV2. Fabricating this clearance is a physical necessity to permit fluid flow through the diode, as if the upper surface and membrane were fabricated with a smaller, or rather no, clearance, the two surfaces would fuse together during 3D printing to form completely isolated upper and lower diode channels, and no through-flow would be permitted. The as-fabricated DiodeV2 operator (with the bracket off) indeed employs the same closure principle as Diode$_{V1}$, that is, that negative fluidic pressure, which induces a necessary degree of reverse fluid flow (i.e., back-flow), is required in order to displace the 3D corrugated membrane upwards until contact is made with the upper surface in order to close the clearance and turn the diode "off".

The idea of employing the modular bracket element is to close the as-fabricated initial clearance between the internal 3D corrugated membrane and the upper surface inside Diode$_{V2}$, such that when installed, the upper surface is deflected down onto the membrane, closing the clearance in the default (static) state, such that under neutral fluid pressures or reverse fluid pressure, the DiodeV2 is "normally closed", by default. To the authors' knowledge, utilizing a modularly fabricated bracket element represents the only approach to realizing a "normally closed" valving element in an otherwise-entirely monolithically fabricated platform.

6.4. A Note on the Effect of Fabricated Surface Roughness on Diode Closure Mechanisms

In the ideal design, a perfect seal would exist between the flat and smooth surfaces in contact, effectively producing an infinitely-high flow rate and permitting zero back-flow. The nature of the fabrication surfaces, however is not ideal, as surface roughness on the order of ∼10's μm [12] exists on both surfaces; thus, when the peaks on the surfaces of each of the parallel surfaces are in contact, the membrane can displace no further upwards, yet a small volume of liquid is likely permitted to flow through the surface roughness peaks.

7. Additional Comparisons Between FPA$_{V1}$, FPA$_{V2}$ & FPA$_{V2,in-line}$ Prototypes

7.1. FPA$_{V1}$ & FPA$_{V2}$ Compared

Comparing the raw flow rate *versus* time plots for the fabricated FPA$_{V1}$ and FPA$_{V2}$ prototype platforms also reveals more detailed information on the characteristics of the pressure waves at the device outlet which are the driving force of the fluid actuation. The peaks on the flow rate plot in the forward direction for each actuation cycle for FPA$_{V1}$ take the shape of sharp peaks with a maximum flow rate of ∼40 μL/min, whereas the peaks for FPA$_{V2}$ are all slightly wider but the maximum flow rate is lower, ∼28 μL/min, ∼50 μL/min. Since all of the fluidic operators are identical between these designs except for the design of the fluidic diodes, this behavior indicates a higher fluidic resistance in the forward direction for Diode$_{V2}$ than for Diode$_{V1}$. Interestingly, the aperture on the membrane in Diode$_{V1}$ is in fact smaller (represented by a clearance of 100 μm, outer diameter of 800 μm, inner diameter of 600 μm and annular area of ∼0.22 mm^2) than the aperture on the membrane in Diode$_{V2}$ (represented by a through-hole diameter of 800 μm and area of ∼0.50 mm^2), and therefore creates a higher fluidic resistance to the fluid flowing through the aperture. The observed overall fluidic resistance behaviors are not in conflict with this fact, however, since the higher fluidic resistance in Diode$_{V2}$ is due to the dynamic closure mechanism employed in the interior. Namely, the as-fabricated clearance between the aperture and the upper surface in the interior of Diode$_{V1}$ provides a lower fluidic resistance in the forward direction than induced by the initial contact made between the aperture and upper surface inside the interior of Diode$_{V2}$ when the bracket is installed onto the exterior of the diode. The higher fluidic resistance in the forward direction in the Diode$_{V2}$ is due to the pressures that the fluid must (*i*) first exert onto the membrane to initially displace the membrane such that fluid can begin to flow through the aperture, followed by that which must resist the restorative force in the membrane, upon each actuation cycle. Therefore, the Diode$_{V2}$ design experiences more of an energy loss per actuation cycle than the Diode$_{V1}$ design.

The advantage of the Diode$_{V2}$ design over the Diode$_{V1}$ design, however, is revealed by the back-flow characteristics of each prototype. The overall back-flow in the system is predominantly due to the back-flow through the right-most diode when the pressure source is instantaneously *turned off* when the finger-actuated membrane is released. Analyzing the flow rate in the reverse direction for each actuation cycle for FPA$_{V1}$, the reverse flow rate adopts a decayed behavior with a maximum reverse flow rate of ∼20 μL/min, suggesting that the pressure drop across the membrane in the reverse direction possesses a restorative response time which is dependent on the mechanical properties of the membrane (*e.g.* elastic modulus). In other words, when the pressure source pressure is released, fluid flows from the device outlet through the lower channel of the right-most diode which flows through the aperture of the membrane. The gap between the membrane and the upper surface of the stationary piston in Diode$_{V1}$ is at a maximum, therefore the fluidic resistance is at a minimum, at this point in time. As the elastic strain in the diode membrane and the vacuum pressure in the upper diode channel from the fluidic reservoir restores the membrane back to its initial position, the fluidic resistance increases and saturates at a specific magnitude limited by the as-fabricated clearance between the membrane and upper surface. As a result, the back-flow in the diode decays is only stopped once the fluidic reservoir is completely filled with fluid and all membranes are restored back to their original

Ratio of Volume Per Push (μL) in Forward to Reverse Directions ($V_{forward}$ / $V_{reverse}$)

FPA design *with* air-fluid cavity (FPA_{v2})

a	Forward Flow (uL)	Standard Dev	Reverse Flow (uL)	Standard Dev
1Hz	14.62	3.13	4.38	0.87
2Hz	11.28	2.53	2.91	0.53
3Hz	12.04	2.05	3.40	0.70
4Hz	8.47	1.87	2.81	0.56

FPA design *without* air-fluid cavity ($FPA_{v2,\text{ in-line}}$)

b	Forward Flow (uL)	Standard Dev	Reverse Flow (uL)	Standard Dev
1Hz	40.71	5.54	7.96	0.82
2Hz	23.86	6.19	4.67	2.03
3Hz	16.98	3.47	2.45	0.57
4Hz	13.88	2.98	2.52	0.62

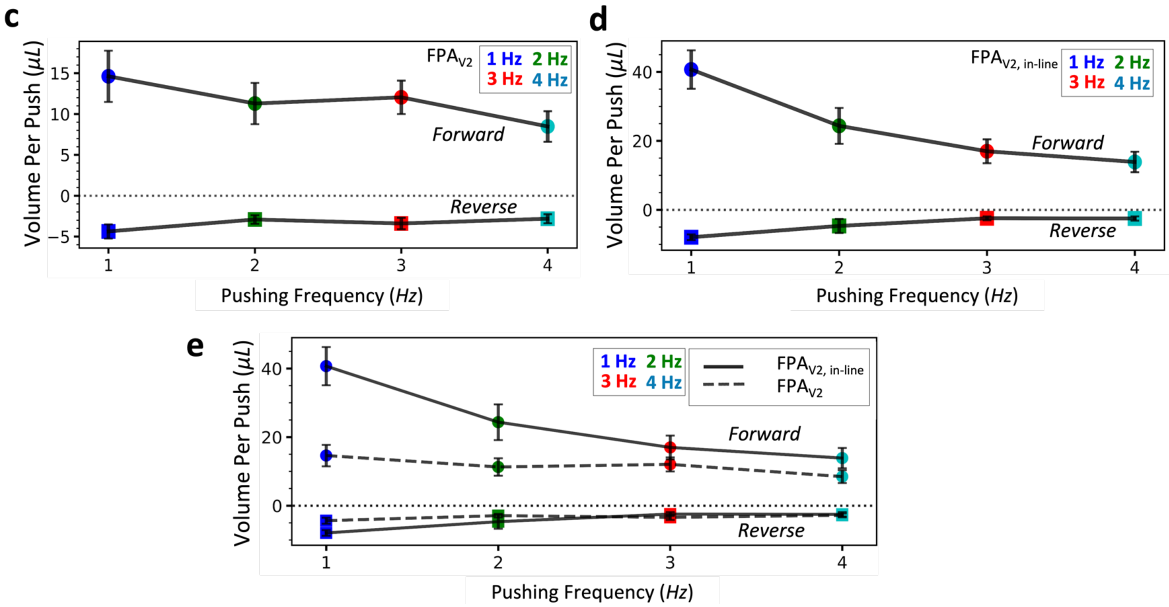

Figure S9. Experimental results for FPA_{V2} and $FPA_{V2,in-line}$ prototypes, ratio of volume per push.

position. As with the case of FPA_{V1} under back-flow, the peak-like behavior observed for the flow rate in the reverse direction for each actuation cycle of FPA_{V2} indicates that some back-flow occurs, but that very soon thereafter, contact is made between the membrane and the displaced upper stationary surface, effectively rectifying flow in the reverse direction with high fluidic resistance.

7.2. *FPA_{V2} & $FPA_{V2,in-line}$ Compared*

Comparisons Between Microchannel Pressures in FPA_{V2} & $FPA_{V2,in-line}$ Prototypes

Moreover, measurements of the pressures generated in both the upper and lower channels of the right-most $Diode_{V2}$ of the fabricated FPA_{V2} and $FPA_{V2,in-line}$ prototypes under both positive and negative pressure conditions reveal further information about the pressure wave created by each prototype design, as well as the effect of the in-line pressure source in the $FPA_{V2,in-line}$ design on the overall fluid output performance. See Table S1 for tabulated maximum fluidic pressure and standard deviations (averages calculated over six independent experimental trials actuating at 1 Hz for 60 seconds) as measured for the right-most diode ($Diode_{V2}$ design; output of the lower channel produces the fluidic output of the device) for the fabricated FPA_{V2} and $FPA_{V2,in-line}$ prototypes with the brackets installed in the upper and lower channels under forward fluid flow (forward-driving pressure portion of the actuation cycle) and under reverse fluid flow (back-flow-driving pressure portion of the actuation cycle) conditions. All pressure measurements were created using the LabSmith pressure sensor (*LabSmith*) and all flow rate measurements were created using the FLOWELL platform fluid flow rate sensors (*Fluigent*). For the FPA_{V2} prototype design with the brackets on, analyzing the right-most diode under *forward flow* conditions, the maximum pressure generated in the *upper channel* is ∼17.1 kPa and in the *lower channel* is ∼8.2 kPa; whereas under *reverse flow* conditions, the maximum pressure generated in the *upper channel* is ∼-7.1 kPa and in the *lower channel* is ∼-2.9 kPa. And for the $FPA_{V2,in-line}$ prototype design with the brackets on, analyzing the right-most diode under *forward flow* conditions, the maximum pressure generated in the *upper channel* is ∼31.4 kPa and in the *lower channel* is ∼22.4 kPa; whereas under *reverse flow* conditions, the maximum pressure generated in the *upper channel* is ∼-11 kPa and in the *lower channel* is ∼-5.4 kPa. These measurements indicate that overall larger pressures in the right-most diode are generated using the in-line pressure source approach demonstrated by the $FPA_{V2,in-line}$ prototype as compared to using the fluid reservoir approach demonstrated by the FPA_{V2} prototype.

		FPA_{V2}		$FPA_{V2,in-line}$	
		Max (kPa)	Stdev (kPa)	Max (kPa)	Stdev (kPa)
Upper Channel	Forward Flow	17.107	5.216	31.353	5.377
	Reverse Flow	-7.062	2.231	-11.010	1.994
Lower Channel	Forward Flow	8.185	2.470	22.423	11.906
	Reverse Flow	-9.925	1.410	-5.409	3.189

Table S1. Mean maximum pressure values, average calculated from *six* experimental trials and standard deviations in units of kPa for FPA_{V2} and $FPA_{V2,in-line}$ prototypes with brackets installed.

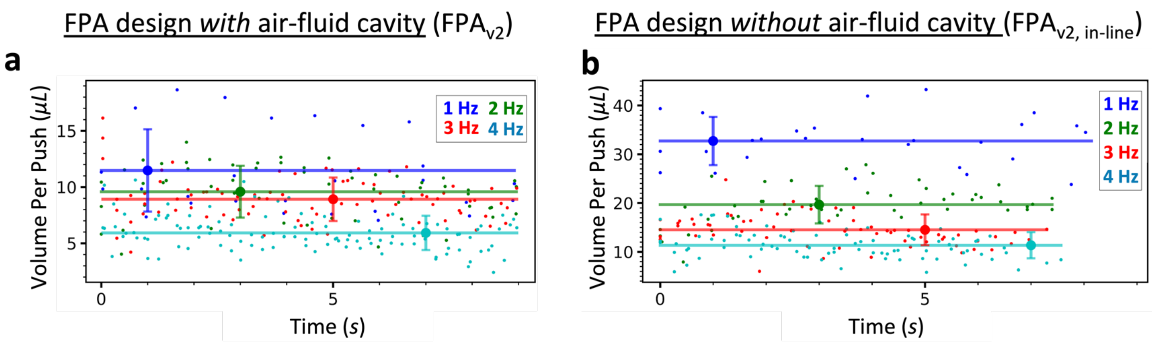

Figure S10. Experimental results for FPA_{V2} and $FPA_{V2,in-line}$ prototypes, average volume per push.

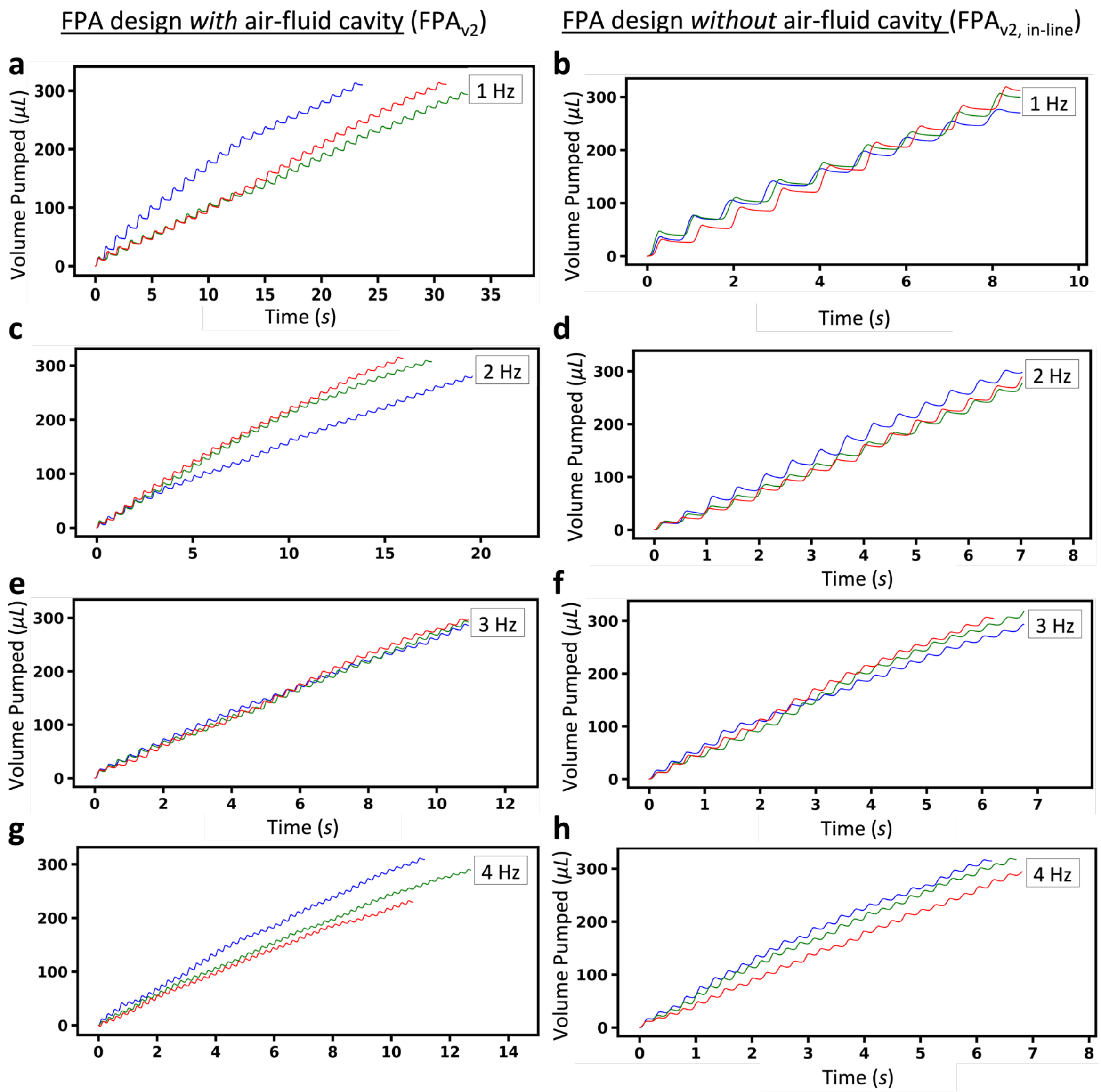

Figure S11. Experimental results for FPA_{V2} and $FPA_{V2,in-line}$ prototypes, volume pumped *versus* time.

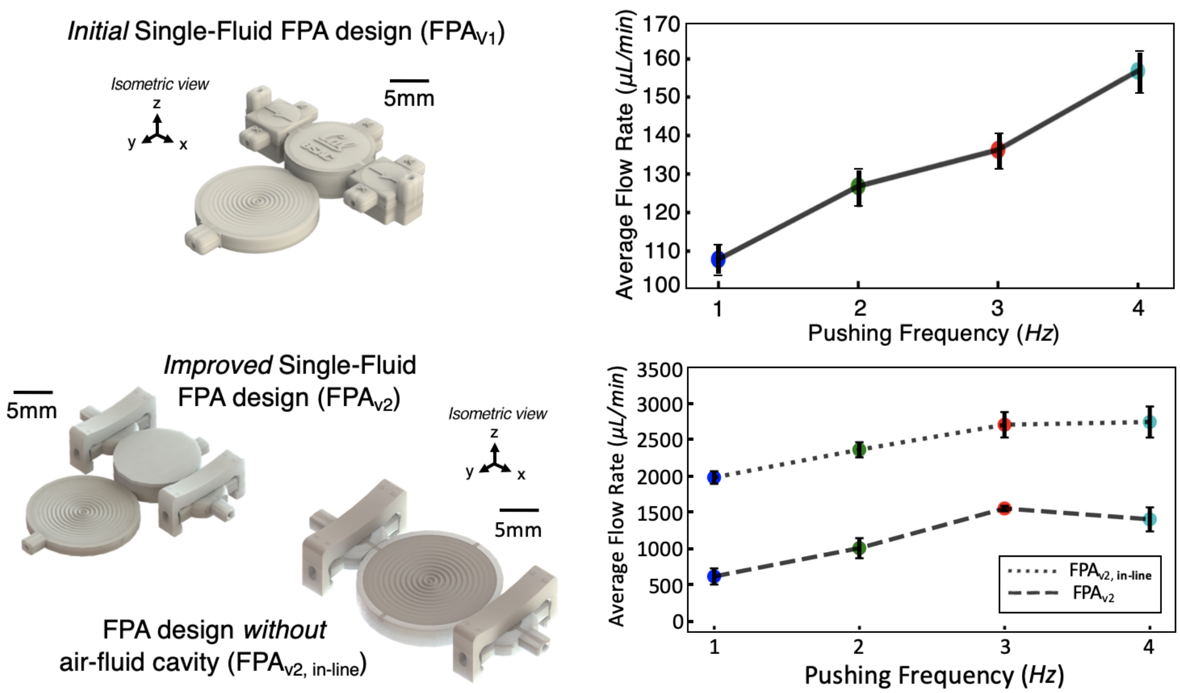

FPA$_{V1}$

Frequency	Mean Flow Rate ($\mu L/min$)	Stand. Dev. ($\mu L/min$)	Stand. Dev. percent of Mean (%)	Device Average Stand. Dev. ($\mu L/min$)	Average Stand. Dev. Perc. of Mean (%)
1 Hz	108	2.25	2.11	**4.56**	**3.34**
2 Hz	126	5	3.91		
3 Hz	136	5	3.60		
4 Hz	156	6	3.75		

FPA$_{V2}$

Frequency	Mean Flow Rate ($\mu L/min$)	Stand. Dev. ($\mu L/min$)	Stand. Dev. percent of Mean (%)	Device Average Stand. Dev. ($\mu L/min$)	Average Stand. Dev. Perc. of Mean (%)
1 Hz	637	97	15.12	**98.63**	**9.78**
2 Hz	1027	125	12.10		
3 Hz	1575	27	1.70		
4 Hz	1450	145.5	10.13		

FPA$_{V2, \text{in-line}}$

Frequency	Mean Flow Rate ($\mu L/min$)	Stand. Dev. ($\mu L/min$)	Stand. Dev. percent of Mean (%)	Device Average Stand. Dev. ($\mu L/min$)	Average Stand. Dev. Perc. of Mean (%)
1 Hz	2000	81	4.12	**141.38**	**5.66**
2 Hz	2378	102	4.37		
3 Hz	2717	174	6.49		
4 Hz	2775	209	7.68		

Figure S12. Summary of the experimental results for average flow rate versus actuation frequency for the fabricated FPA$_{V1}$, FPA$_{V2}$ and FPA$_{V2,in-line}$ prototypes. Standard deviation (stand. dev.) between three distinct experimental trials for each data point are tabulated in the tables at the bottom of the figure. Device average stand. dev. across all four actuation frequencies are shown.

7.3. Further Discussion on the Variability and Repeatability of the Fabricated Prototype FPA Devices

Discussion of the Standard Deviation of Experimental Data for All Prototypes

In order to further consider the variability of the experimental data collected during experimental characterization of all fabricated prototypes, Figure S12 summarizes the experimental average flow rate versus actuation frequency data for the fabricated FPA_{V1}, FPA_{V2} and $FPA_{V2,in-line}$ prototypes, as well as tabulates the standard deviation (stand. dev.) between the three distinct experimental trials performed for each data point for each prototype. The tables at the bottom of the figure illustrate that the average device standard deviation, i.e., the variability in the output flow rate performance for the specific device, operation-to-operation, between all operational frequencies for the FPA_{V1}, FPA_{V2} and $FPA_{V2,in-line}$ prototypes is ∼3.34%, ∼9.78% & ∼5.66%, respectively. Since the fabricated FPA devices have the capability to generate on average an output flow rate which is within, and depending on the FPA design much lower than, ∼10%, these devices demonstrate practicality in reliability towards real-world sub-millifluidic and microfluidic actuation applications.

Discussion of the Repeatability of All Prototype Designs

In analyzing the repeatability of each of the fabricated prototypes featured in this work, repeatability can be considered in two distinct contexts: (i) the cyclical repeatability for a specific device, i.e., the consistency in the magnitude of output flow rate generated at a single frequency during a single operational run; and (ii) the operation-to-operation repeatability, or reusability, i.e., the ability of for the device to perform with minimal variation at different actuation frequencies during independent experimental operational runs.

Considering the cyclical repeatability of each device, the effect of cycle-to-cycle actuation variation can be seen in Figure S10a,b for the FPA_{V2} and $FPA_{V2,in-line}$ prototypes. Each plot presents the combined raw volume pumped versus time data for three individual experimental operations at frequencies from 1-4 Hz. As is evident, the net-forward fluid volume actuated out of the device per-push with time for a period of roughly 9 seconds demonstrates cycle-to-cycle variation, for example, actuation of both prototypes at 1 Hz produces net-forward fluid volume per-push anywhere fro roughly 25 μL/min to above 40 μL/min. As the cyclical actuation frequency increases from 1-4 Hz, the cycle-to-cycle variation slightly decreases. One of the most likely sources of cycle-to-cycle variation lies in the inherent inconsistency in the applied force from the human operator via the finger-actuated membrane, i.e., manual distance of membrane displacement. During operation, the operator is meant to displace the finger-actuated membrane until no further displacement can be achieved, i.e., the bottom surface of the 3D corrugated membrane touches the flat top surface of the interior of the finger-powered pressure chamber. If, however, the operator were to not entirely displace the membrane to its fullest extent, the pressure generated in the control channel on that actuation cycle would be less than the maximum achievable pressure, resulting in such an inconsistency. Alternatively, if the operator were to actuate the membrane with imprecision, i.e., actuating at plus or minus ∼0.5 Hz or so from the intended actuation frequency, let alone an inconsistent imprecision throughout an operation, the resulting variation in performance could be well explained. As no noticeable and repeatable trend in the increase or decrease in the actuation variation is exhibited by either prototype device during actuation at any frequency (i.e., if the variation in output flow rate uniformly increases or decreases in magnitude from cycle-to-cycle during the course of a single operational trial), it is surmised that the cyclic repeatability is likely more to due with the inconsistency in operator actuation force and frequency, rather than due to any effects of material plastic deformation or changing material responsiveness, i.e., material fatigue, during operation.

Furthermore, considering the operation-to-operation repeatability of the fabricated prototypes, Figure S11a-h demonstrates the observed variations in net-volume actuated out of the device over time for 1-4 Hz for both the FPA_{V2} and $FPA_{V2,in-line}$ designs. As is evident, for example in Figure S11a,c,g, variations in the FPA_{V2} device output performance for three individual experimental operations at 1, 2 and 4 Hz resulted in higher net-volume actuated over time in one trial than in the two other trials; where as, a comparatively more repeatable performance with reduced operation-to-operation variability is observed in Figure S11e for the FPA_{V2} device actuated at 3 Hz. The experimental results for the $FPA_{V2,in-line}$ design featured in Figure S11b,d,f,h reveal a similar pattern, with slightly higher operation-to-operation variability at 2 Hz and 4 Hz but with more repeatable behavior at 1 Hz and 3 Hz. In ascertaining the potential reasons for such observed operation-to-operation repeatability, or lack-thereof in specific demonstrations, one potential consideration could be the result of a physical manifestation, i.e., plastic deformation of any physical dynamic elements or changes in the material responsiveness during operation. If this were the case, however, the expectation would be to observe a noticeable and constant change in the performance of each device over the course of multiple operations at a specific actuation frequency. For example, during operation if the 3D printed corrugated membranes were to have experienced plastic deformation in the material or otherwise irreversible physical damage, e.g., fractures in the membrane causing leaking, in theory the 3D corrugated membranes would have reduced responsiveness due to more flexible material with less capability to store recoverable elastic strain energy, therefore a discernible reduction in device output volume pumped with time over subsequent operations would be expected, such as was the trend observed for the FPA_{V2} device actuated at 1 Hz (Figure S11a) and the $FPA_{V2,in-line}$ device actuated at 2 Hz (Figure S11d). The opposite trend is observed, however, in every other experimental trial. Moreover, the same fabricated devices were used to collect the experimental results for all operations from 1-4 Hz. As a result, if the aforementioned potential physical manifestations were to be responsible for the variation in the repeatability of any device's performance (i.e., material weakness over time causes less volume to be actuated at higher frequencies), a discernible decrease in device performance would be observed between operations at higher actuation frequencies. For each device, however, the net-forward volume pumped does not decrease reliably as actuation frequency increases for all twelve experimental trials of both prototype designs; therefore, the most likely source of the operation-to-operation variability is, similar to the cycle-to-cycle repeatability, likely more to due with the inconsistency in operator actuation force and frequency. On that note, regarding the longevity of the 3D printed dynamic membranes featured in this work, the complete set of experimental trials involving each fabricated prototype, i.e., three experimental trials per actuation frequency for 1-4 Hz, were performed over the course of approximately five days of experiments performed throughout the week per-prototype. In the context of the experiments performed in this work, no discernible degradation in device performance or visible plastic deformation in the dynamic membranes were observed for any of the fabricated prototypes.

Finally, the variability of each of the device designs compared to one another can be considered in order to ascertain the effect of device design on repeatability by considering the standard deviation of the mean flow rate for each device as presented in Figure S12. The highest and lowest operation-to-operation variation for the FPA_{V1} prototype are exhibited at 2 Hz (∼3.91 μL/min) and 1 Hz (∼2.11 μL/min), respectively; for the FPA_{V2} prototype at 1 Hz (∼15.12 μL/min) and 3 Hz (∼1.70 μL/min), respectively; and for the $FPA_{V2,in-line}$ prototype at 1 Hz (∼4.12 μL/min) and 4 Hz (∼7.68 μL/min), respectively. One potential explanation for why FPA_{V2} demonstrates higher operation-to-operation variability than FPA_{V1} could be that the $Diode_{V2}$ designs permit less back-flow through the system than the $Diode_{V1}$ designs; as a result, the $Diode_{V2}$ designs are more sensitive to slight variations in the magnitude and/or frequencies of the forward driving fluid pressure waves generated by the finger-powered pressure source than the $Diode_{V1}$ designs, which permit a fair degree of back-flow, dampening out such slight variations in the forward driving fluid pressure waves. In comparison, $FPA_{V2,in-line}$ generates smaller operation-to-operation variation than FPA_{V2}, likely due the significantly higher forward driving fluid pressures, which are sufficiently large as to overwhelm such slight variations in the forward driving fluid pressure wave.

8. Discussion on the Restorative Behavior of the 3D Corrugated Membranes Per-Actuation Cycle

As was observed during experimental characterization of each fabricated prototype FPA device, the output fluid flow dynamics is pulsatile in nature, in that period peaks for forward flow rate out of the device, followed by troughs of reverse flow rate (back-flow) into the device, are observed. In what could be thought of as an ideal FPA system, the 3D fluidic diodes would fully close in the reverse direction upon instantaneous reversal of fluid pressure inside the diode channels ($\Delta P<0$), resulting in a complete absence of back-flow through the system. In this situation, upon each push of the finger-actuated membrane, the 3D corrugated membrane in the fluidic reservoir would expand upwards, forcing through the right-most fluidic diode with a peak output flow rate. When the finger-actuated membrane is released, the elastic recovery of the 3D corrugated membranes inside the finger-powered pressure source and fluidic reservoir would restore the membranes back to their original position, creating a positive pressure in the left-most fluidic diode and draw source fluid through the diode and into the fluidic reservoir. In the realistic situation, however, the elastic strain energy due to the downward deflection of the 3D corrugated membranes inside each fluidic diode under positive forward pressure ($\Delta P>0$) and restorative force under negative forward pressure ($\Delta P<0$), results in an inherent degree of back-flow in the system, albeit which is much more significantly reduced by the design of Diode$_{V2}$ as compared to Diode$_{V1}$.

The restorative behavior of the 3D corrugated membranes is therefore an important driving factor in the overall device performance. For instance, when considering the output flow rate characteristics of the prototype FPA$_{V1}$ device, as shown in Figure S6, the reverse flow rate due to back-flow exhibits a gradual decayed behavior, with a maximum reverse flow rate of $\sim$20 μL/min, and asymptotically settles at $\sim$0 μL/min. This decayed back-flow is inherent to the restorative response time of the 3D corrugated membrane inside the fluidic diode, whereby when $\Delta P<0$ inside the diode after each push, the energy stored in the displaced membrane due to elastic strain stored in the membrane structure restores the membrane back to its initial position. The degree of elastic energy stored in the membrane and the degree of deflection of the membrane is dependent on the mechanical properties of the membrane, most predominantly the stiffness of the material, and its geometric parameters, including the thickness, the 3D corrugated geometry and the diameter of the membrane [13]. In this work, the structural material used is the urethane-based Visijet M3 crystal (*3D Systems*) polymer. This material, when cured, is mechanically rigid with an elastic modulus given in the material data sheet as 1.159 GPa [14]; however as previous work from our group has demonstrated, the elastic modulus has been experimentally found to lower, roughly 58-116 MPa [15]. When cured, the polymer has proven sufficiently ductile to produce robust deformable thin-walled mechanical 150 μm-thick membranes, however, capable of repeatable deformations simply using manual force applied by a human finger [9,16,17]. This characteristic of the otherwise-mechanically stiff material lent the 3D corrugated membranes designed and implemented in the FPA devices the flexibility necessary to act as deformable and restorative membranes to generate the fluidic actuation featured in this work.

In regards to the relative deformability of all of the membranes featured in the FPA designs, the finger-actuated (20mm diameter), adjustable fluidic capacitor (15mm diameter) and fluidic diode (7mm diameter) membranes feature decreasing magnitudes of flexibility, and therefore are capable of storing decreasing amounts of elastic energy when displaced, due to their decreasing diameters. As a result, the restorative time of the finger-actuated membrane is the longest, followed by the adjustable fluidic capacitor membrane and lastly the fluidic diode membrane. The consequences of the restoration time of the membranes, i.e., how readily the membranes return to their original states after a push, on the overall device performance is observed in the experimental results for all single-fluid FPA designs. For example, given actuation of FPA$_{V1}$ (Figure S6), at 1 Hz the gradually decayed back-flow to $\sim$0 μL/min indicates that the restorative time of the finger-actuated membrane at or below 1 second, as by the end of each actuation cycle, the full volume of the fluidic reservoir is restored. Indeed, this behavior was observed qualitatively by the operator responsible for performing the experiments, as less membrane displacement was noticeable with increasing operational frequencies per-actuation cycle upon depression of the finger-actuated membrane. Furthermore, when depressing the finger-actuated membrane completely, then releasing the finger to observe the restoration of the membrane, it was observed that the membrane visually appeared to fully restore to its original position at approximately 1 second.

As the actuation frequency is increased from 2-4 Hz, however, the characteristic asymptotic decay in back-flow is not observed; rather, an increasingly symmetric periodic forward-reverse flow rate behavior is observed, likely the result of imperfect closure of the 3D membranes inside the fluidic diodes in the Diode$_{V1}$ designs even after they restore to their static positions. In addition, as was consistent for the FPA$_{V2}$ and FPA$_{V2,in-line}$ prototype experimental characterizations (Figure S9), at higher frequencies up to 4 Hz, less volume is actuated in the net-forward direction per-actuation cycle. These results indicate that at 2 Hz and higher frequencies, not all of the membranes inside the devices have sufficient time to completely restore to their static positions. Ultimately, in estimation of the restorative time of the finger-actuated membrane, which is the limiting factor for the restorative time of the overall fluidic system, the time required for the membrane to completely restore to its static, as-fabricated position would be on the order of 1 second. However, as even at 250 milliseconds, the period of the 4 Hz actuation operation, since positive volume is actuated in the forward direction for all FPA designs, the partial restorative time, that is the time required for the membrane to release an effective degree of elastic strain energy and restore its displacement in part, is on the order of 250 milliseconds, possibly even shorter.

9. Methods to Further Tailor FPA Device Output Fluid Flow Characteristics

9.1. Approaches to Modify the Designs of Individual Fluidic Circuitry Elements

Finally, in microfluidic device applications where as little back-flow as possible can be permitted yet lower effective fluid flow rates are required, to reduce the overall output flow rate from either the FPA$_{V2}$ or FPA$_{V2,in-line}$ designs (beneficial as they both utilize the Diode$_{V2}$ designs) can be accomplished by adding extra lengths of tubing to the end of the device to increase fluidic resistance of the interfacing hardware; highly-compact 3D printed resistor designs could be integrated into the body of the prototypes themselves at the outlet of the device to increase the pressure drop before the device outlet and therefore decrease the overall output flow rate; either devices could be operated at smaller actuation frequencies (*e.g.* 0.5 or 0.25 Hz); and perhaps most rigorously, certain parameters of the 3D fluidic operators themselves can be redesigned to produce smaller flow rates at the same pumping frequencies. Regarding the latter option, from the ideal gas law, $P_1 * V_1 = P_2 * V_2$, where P_1 is equivalent to the initial starting pressure, $P_0 = P_{atmospheric}$; V_1 is equivalent to the as-fabricated volume of the pressure source cavity, V_0; P_2 is equivalent to the total pressure differential induced by the pressure source, $P_{max}+P_0$; and V_{min} is equivalent to the minimum volume inside the pressure source chamber when the membrane is depressed, which in the devices developed in this work is the result of the non-working air volume contained underneath the 3D corrugated microstructures comprising the finger-actuated membrane and is much smaller than V_1. **Eq. 2c** can be used to relate the maximum pressure generated by the pressure source to the volume change of the finger-actuated membrane,

$$(P_{max} + P_0) * V_{min} = P_0 * V_0 \tag{2a}$$

$$P_{max} + P_0 = \frac{P_0 * V_0}{V_{min}} \tag{2b}$$

$$P_{max} = (\frac{V_0}{V_{min}} - 1) * P_0 \tag{2c}$$

The as-fabricated volume of the hollow pressure cavity in this work (V_0) can be approximated by the volume of a spherical cap, $V_0 = \frac{1}{6}\pi h(3a^2 + h^2)$ where a is the radius of the base of the cap and h is the height of the cap, and is therefore a function of the diameter and thereby area of the finger-actuated pumping membrane. Therefore smaller membrane diameters and thereby smaller V_0 values, assuming the membrane can still be depressed to contact the bottom of the hollow cavity and keeping V_{min} constant, will result in smaller generated values of P_{max}, therefore slower device output flow rates. Likewise, larger membrane diameters and thereby larger V_0 values will result in larger generated values of P_{max}, therefore faster device output flow rates.

9.2. How to Achieve More Approximately Steady-State Fluid Flow Rates

In microfluidic applications which demand steady-state fluid flow rates (i.e. non-pulsatile fluid flow, as demonstrated by the FPA$_{V1,2fluid}$ prototype), the FPA fluidic network design can be modified to deliver a more steady fluid output flow rate via incorporation of 3D fluidic capacitor operators at the device outputs. If manufactured as a modular system, a proposed FPA device can either be designed with integrated, monolithically fabricated 3D fluidic capacitor operators positioned after the right-most diode, serving as the outlet of the device. Alternatively, modular fabricated 3D fluidic capacitor operator prototypes can be assembled onto the outlet microchannel of an FPA prototype, interfacing via tubing and stainless steel couples. Doing so would which serve to dampen the oscillatory pressure wave driving the output fluid flow. The characteristics of the 3D fluidic capacitor operators could be modified to deliver a custom degree of fluid dampening. Such an approach for 3D printed fluidic operators was first proposed by our group in Ref. [9].

9.3. How to Achieve Non-Equivalent Fluid Flow Rates in Two-Fluid FPA Devices

In two-fluid microfluidic examples where *non-equivalent* forward-driven flow rates are desired from each of the fluids, the flow rates generated from each of the independent fluid channels can be altered with respect to one another by changing the size of the membranes inside each of the respective fluid reservoirs. Equation 2c reveals that the numerical estimation of the generated pressure head from the finger-powered pressure source can be tailored by changing the as-fabricated volume of the pressure source cavity. Likewise, the pressure generated inside each *fluid reservoir* can be numerically determined using Equation 2c as well, where V_0 represents the as-fabricated volume of the fluid reservoir, V_{min} represents the minimum volume inside the fluid reservoir when the internal membrane is displaced to its maximum extent upwards into the fluid channel (which can be minimized by designing an upper surface which reflects a spherical cap geometry similar to the lower surface of the pressure source chamber), P_0 represents the initial (at-rest) fluidic pressure inside the fluid chamber, and P_{max} is the maximum fluidic pressure generated in the fluidic channel from the volume reduction of the fluid reservoir. The extent to which the internal membrane displaces upwards into the fluid reservoir, and therefore as a result the generated maximum fluidic pressure, is dependent on the force on the internal membrane generated by the pressure exerted on the membrane from the pressure source channel. The force on the membrane can be related to the force applied to the finger-actuated pressure source membrane using Equation 3c,

$$P_{psm} = P_{frm} \tag{3a}$$

$$\frac{F_{psm}}{A_{psm}} = \frac{F_{frm}}{A_{frm}} \tag{3b}$$

$$F_{frm} = \frac{A_{frm}}{A_{psm}} * F_{psm} \tag{3c}$$

where P_{psm} represents the pressure generated in the pressure source by the deflection of the finger-actuated membrane, P_{frm} represents the pressure exerted in the lower channel of the pressure source air channel on the bottom of the membrane contained in the fluid reservoir, F_{frm} is the force exerted on the fluid reservoir membrane, F_{psm} is the force exerted on the finger-actuated pressure source membrane, A_{frm} is the area of the fluid reservoir membrane and A_{psm} is the area of the finger-actuated pressure source membrane. Therefore by Equation 3c, reducing the area of the fluid reservoir membrane relative to area of the finger-actuated pressure source membrane will reduce the force on the fluid reservoir membrane and therefore the overall fluid flow rate in that specific fluidic channel. In a two-fluid channel setup, reducing the area of one fluid reservoir membrane to the other will reduce the overall output fluid flow rate in that specific fluidic channel to the other fluidic channel.

References

1. Tran Minh, N.; Dong, T.; Karlsen, F. An efficient passive planar micromixer with ellipse like micropillars for continuous mixing of human blood. *Computer Methods and Programs in Biomedicine* **2014**, *117*, 20–29. doi:10.1016/j.cmpb.2014.05.007.
2. Rafeie, M.; Welleweerd, M.; Hassanzadeh-Barforoushi, A.; Asadnia, M.; Olthuis, W.; Warkiani, M.E. An easily fabricated three dimensional threaded lemniscate shaped micromixer for a wide range of flow rates. *Biomicrofluidics* **2017**, *11*, 014108. doi:10.1063/1.4974904.
3. Yasui, T.; Omoto, Y.; Osato, K.; Kaji, N.; Suzuki, N.; Naito, T.; Okamoto, Y.; Tokeshi, M.; Shamoto, E.; Baba, Y. Confocal Microscopic Evaluation of Mixing Performance for Three Dimensional Microfluidic Mixer. *Analytical Sciences* **2012**, *28*, 57. doi:10.2116/analsci.28.57.
4. Lin, Y.C.; Chung, Y.C.; Wu, C.Y. Mixing enhancement of the passive microfluidic mixer with J-shaped baffles in the tee channel. *Biomedical Microdevices* **2007**, *9*, 215–221. doi:10.1007/s10544-006-9023-5.
5. Fang, W.F.; Yang, J.T. A novel microreactor with 3D rotating flow to boost fluid reaction and mixing of viscous fluids. *Sensors and Actuators, B: Chemical* **2009**, *140*, 629–642. doi:10.1016/j.snb.2009.05.007.
6. Mansur, E.A.; Ye, M.; Wang, Y.; Dai, Y. A State of the Art Review of Mixing in Microfluidic Mixers. *Chinese Journal of Chemical Engineering* **2008**, *16*, 503–516. doi:10.1016/S1004954108601147.
7. Hashmi, A.; Xu, J. On the Quantification of Mixing in Microfluidics. *Journal of Laboratory Automation* **2014**, *19*, 488–491. doi:10.1177/2211068214540156.
8. Locascio, L.E. Microfluidic mixing. *Analytical and Bioanalytical Chemistry* **2004**, *379*, 325–327. doi:10.1007/s00216-004-2630-1.
9. Sochol, R.D.; Sweet, E.; Glick, C.C.; Venkatesh, S.; Avetisyan, A.; Ekman, K.F.; Raulinaitis, A.; Tsai, A.; Wienkers, A.; Korner, K.; Hanson, K.; Long, A.; Hightower, B.J.; Slatton, G.; Burnett, D.C.; Massey, T.L.; Iwai, K.; Lee, L.P.; Pister, K.S.; Lin, L. 3D printed microfluidic circuitry via multijet-based additive manufacturing. *Lab on a Chip* **2016**, *16*, 668–678. doi:10.1039/c5lc01389e.
10. Pourmand, A.; Shaegh, S.A.M.; Ghavifekr, H.B.; Najafi Aghdam, E.; Dokmeci, M.R.; Khademhosseini, A.; Zhang, Y.S. Fabrication of whole-thermoplastic normally closed microvalve, micro check valve, and micropump. *Sensors and Actuators, B: Chemical* **2018**, *262*, 625–636. doi:10.1016/j.snb.2017.12.132.
11. Mosadegh, B.; Agarwal, M.; Tavana, H.; Bersano-Begey, T.; Torisawa, Y.s.; Morell, M.; Wyatt, M.J.; O'Shea, K.S.; Barald, K.F.; Takayama, S. Uniform cell seeding and generation of overlapping gradient profiles in a multiplexed microchamber device with normally-closed valves. *Lab Chip* **2010**, *10*, 2959–2964. doi:10.1039/C0LC00086H.
12. Sochol, R.D.; Sweet, E.; Glick, C.C.; Wu, S.Y.; Yang, C.; Restaino, M.; Lin, L. 3D printed microfluidics and microelectronics. *Microelectronic Engineering* **2018**, *189*, 52–68. doi:10.1016/j.mee.2017.12.010.
13. Schomburg, W.K. Introduction to Microsystem Design **2011**. *1*. doi:10.1007/978-3-642-19489-4.
14. 3D Systems. VisiJet M3 Crystal. *Material Data Sheet* **2016**, *1*, 1–7.
15. Glick, C.C.; Srimongkol, M.T.; Schwartz, A.J.; Zhuang, W.S.; Lin, J.C.; Warren, R.H.; Tekell, D.R.; Satamalee, P.A.; Lin, L. Rapid assembly of multilayer microfluidic structures via 3D printed transfer molding and bonding. *Microsystems and Nanoengineering* **2016**, *2*, 16063. doi:10.1038/micronano201663.
16. Sweet, E.C.; Mehta, R.R.; Lin, R.; Lin, L. Finger powered, 3D printed microfluidic pumps. *TRANSDUCERS 2017 19th International Conference on Solid-State Sensors, Actuators and Microsystems* **2017**, pp. 1766–1769. doi:10.1109/TRANSDUCERS.2017.7994410.
17. Sweet, E.C.; Liu, N.; Chen, J.; Lin, L. Entirely-3D Printed Microfluidic Platform for on-Site Detection of Drinking Waterborne Pathogens. *Proceedings of the IEEE International Conference on Micro Electro Mechanical Systems (MEMS)* **2019**, pp. 79–82.